LA-UR-11-11505 - 9/29/2011 DRAFT for Submission

Observation and Spectral Measurements of the Crab Nebula with Milagro

A. A. Abdo,[1,2] B. T. Allen,[3,4] T. Aune,[5] W. Benbow,[18] D. Berley,[6] C. Chen,[3] G. E. Christopher,[7] T. DeYoung,[8] B. L. Dingus,[9] R. W. Ellsworth,[10] A. Falcone,[8] L. Fleysher,[7] R. Fleysher,[7] M. M. Gonzalez,[11] J. A. Goodman,[6] J. B. Gordo,[19] E. Hays,[12], C. M. Hoffman,[9] P. H. Hüntemeyer,[13] B. E. Kolterman,[7] J. T. Linnemann,[1] J. E. McEnery,[12] T. Morgan,[14] A. I. Mincer,[7] P. Nemethy,[7] J. Pretz,[9] J. M. Ryan,[14] P. M. Saz Parkinson,[5] A. Shoup,[15] G. Sinnis,[9] A. J. Smith,[6] V. Vasileiou,[6,16] G. P. Walker,[9,17] D. A. Williams[5] and G. B. Yodh[3]

ABSTRACT

The Crab Nebula was detected with the Milagro experiment at a statistical significance of 17 standard deviations over the lifetime of the experiment. The experiment

[1] Department of Physics and Astronomy, Michigan State University, 3245 BioMedical Physical Sciences Building, East Lansing, MI 48824

[2] Current address: Space Science Division, Naval Research Laboratory, Washington, DC 20375

[3] Department of Physics and Astronomy, University of California, Irvine, CA 92697

[4] Current address: Harvard-Smithsonian Center for Astrophysics, Cambridge, MA 02138

[5] Santa Cruz Institute for Particle Physics, University of California, 1156 High Street, Santa Cruz, CA 95064

[6] Department of Physics, University of Maryland, College Park, MD 20742

[7] Department of Physics, New York University, 4 Washington Place, New York, NY 10003

[8] Department of Physics, Pennsylvania State University, University Park, PA 16802

[9] Group P-23, Los Alamos National Laboratory, P.O. Box 1663, Los Alamos, NM 87545

[10] Department of Physics and Astronomy, George Mason University, 4400 University Drive, Fairfax, VA 22030

[11] Instituto de Astronomía, Universidad Nacional Autónoma de México, D.F., México, 04510

[12] NASA Goddard Space Flight Center, Greenbelt, MD 20771

[13] Department of Physics, University of Utah, Salt Lake City, UT 84112

[14] Department of Physics, University of New Hampshire, Morse Hall, Durham, NH 03824

[15] Ohio State University, Lima, OH 45804

[16] CRESST NASA/Goddard Space Flight Center, MD 20771 and University of Maryland, Baltimore County, MD 21250

[17] Current address: National Security Technologies, Las Vegas, NV 89102

[18] Harvard-Smithsonian Center for Astrophysics, Cambridge, MA 02138

[19] Departmento de Fśica, Universidad de Murcia, E-30100 Murcia, Spain

was sensitive to approximately 100 GeV - 100 TeV gamma ray air showers by observing the particle footprint reaching the ground. The fraction of detectors recording signals from photons at the ground is a suitable proxy for the energy of the primary particle and has been used to measure the photon energy spectrum of the Crab Nebula between ∼1 and ∼100 TeV. The TeV emission is believed to be caused by inverse-Compton up-scattering scattering of ambient photons by an energetic electron population. The location of a TeV steepening or cutoff in the energy spectrum reveals important details about the underlying electron population. We describe the experiment and the technique for distinguishing gamma-ray events from the much more-abundant hadronic events. We describe the calculation of the significance of the excess from the Crab and how the energy spectrum is fit. The excess from the Crab is fit to a function of the form

$$\frac{dN}{dE}(I_0, \alpha, E_{\rm cut}) = I_0(\frac{E}{E_0})^{-\alpha} \exp(\frac{-E}{E_{\rm cut}})$$

where the flux I_0, spectral index α and exponential cutoff energy $E_{\rm cut}$ are allowed to vary and E_0 is chosen to de-correlate the fit parameters. The energy spectrum, including the statistical errors from the fit, obtained using the simple power law hypothesis, that is $E_{cut} = \infty$, for data between September 2005 and March 2008 is:

$$\frac{dN}{dE} = (6.5 \pm 0.4) \times 10^{-14}(E/10\ {\rm TeV})^{-3.1\pm0.1}({\rm cm}^2\ {\rm sec\ TeV})^{-1}$$

between ∼1 TeV and ∼100 TeV. When a finite E_{cut} is fit the result is

$$\frac{dN}{dE} = (2.5^{+0.7}_{-0.4}) \times 10^{-12}(E/3\ {\rm TeV})^{-2.5\pm0.4} \exp(-E/32^{+39}_{-18}\ {\rm TeV})({\rm cm}^2\ {\rm sec\ TeV})^{-1}$$

The results are subject to an ∼30% systematic uncertainty in the overall flux and an ∼0.1 in the power law indicies quoted. Uncertainty in the overall energy scale has been absorbed into these errors.

Fixing the spectral index to values that have been measured below 1 TeV by IACT experiments (2.4 to 2.6), the fit to the Milagro data suggests that Crab exhibits a spectral steepening or cutoff between about 20 to 40 TeV.

Subject headings: gamma rays: observations — pulsars: general — pulsar wind nebulae — Crab Nebula

1. Introduction

The Crab supernova remnant is a luminous nearby VHE gamma-ray source created by a 1054 CE supernova observed on Earth by Chinese, Arab and native American astronomers. The optically luminous shell is easily visible from Earth. The Crab Nebula lies 2 kpc from the Earth and is powered by a 33 ms pulsar that injects relativistic electrons into the nebula. The central pulsar

and its surrounding nebula are among the most widely studied astronomical objects across the entire electromagnetic spectrum. A population of energetic electrons is created by the conversion of rotational kinetic energy of the neutron star and acceleration in the shock formed where this flow reaches the surrounding medium. These electrons can interact by the inverse-Compton process with the associated synchrotron photons to create the multi-TeV gamma rays that have been seen (Gaensler & Slane 2006).

Despite the recent flares in 100 MeV - 100 GeV emission observed in AGILE (Tavani et al. 2011) and the Fermi-LAT (Abdo et al. 2011) and in the TeV by ARGO-YBJ (Aielli et al. 2010), the TeV emission from the Crab is believed to be steady when observed over several months and is a standard reference source for comparison to other TeV instruments. Such comparisons are useful as a cross-calibration of the various ground telescopes. The Crab was first detected at TeV energies by the Whipple telescope in 1989 (Weekes et al. 1989). Imaging Atmospheric Cherenkov Telescopes (IACTs) (Aharonian et al. 2004, 2006; Celik 2008; Aliu et al. 2008) and extensive air-shower (EAS) ground arrays (Atkins et al. 2003; Amenomori et al. 2009; Bartoli et al. 2011) have been used to identify and measure the flux of the TeV emission from the Crab. Since the size of the Crab nebula is small compared to the point spread function of TeV gamma-ray detectors, the emission region appears point-like, and study of the Crab can serve as a calibration of an instrument's pointing and angular resolution.

The Milagro experiment (Atkins et al. 2003; Abdo et al. 2009) was a large water-Cherenkov detector sensitive to energetic secondary particles in the particle shower resulting when a high-energy gamma ray or cosmic ray strikes the atmosphere. The experiment was able to distinguish gamma-ray-induced showers from hadron-induced showers by measuring the penetrating component characteristic of hadronic particle showers. The experiment was sensitive to EAS resulting from primary gamma rays between 100 GeV and 100 TeV and has dynamic range to resolve gamma-ray energy spectra between about 1 and 100 TeV. The experiment operated nearly 24 hours a day and viewed the entire overhead sky. The detector was located at 106.68^oW longitude, 35.88^oN latitude in northern New Mexico at an altitude of 2630 m above sea level and operated from 2000 to 2008. The sensitive area of the detector comprised two parts: a central water reservoir and an "outrigger" array of water tanks, both instrumented with 8-inch hemispherical photomultiplier tubes (PMTs) manufactured by Hamamatsu (Model R5912). The central reservoir was operated alone from 2000 to 2004 when the outrigger array was added. The central Milagro reservoir consisted of two PMT layers (Atkins et al. 2000) deployed in a 60x80x8-meter covered water reservoir. The outrigger array consisted of 175 water tanks each with a single PMT mounted at the top of the tank and observing downward into the water of the Tyvek-lined tank. The outrigger tanks were spread in an irregular pattern over an area of 200x200 meters around the central reservoir. The PMTs detected Cherenkov radiation produced in the water by the high-energy particles in an extensive air shower (EAS) that reached to ground level. The Milagro experiment has previously reported TeV emission from the Crab (Atkins et al. 2003) prior to the addition of the Milagro outriggers. With the greater sensitivity from the outriggers and additional exposure, measurement of an energy spectrum is

possible. The direction of the primary particle in an EAS was estimated using the arrival time of the PMT signals. The angular resolution of Milagro, defined as the standard deviation, σ, of a two-dimensional Gaussian fit to the angular error distribution, varied between about 1.2 and 0.35 degrees for the data presented here. The angular resolution is a function of both the size of the event, and the operational period of the detector.

Since higher-energy primary particles result in characteristically larger events on the ground, we use a measure of size of the events on the ground to measure the spectrum of the Crab, constraining emission out to 100 TeV. In section 2, we describe the background estimation and the construction of "skymaps". Section 3 describes the event energy estimation and spectral fitting. In section 4, we verify our energy reconstruction using cosmic-ray hadrons and finally compute the flux and the spectrum of the Crab from 1 to 100 TeV.

2. Skymaps and Background Estimation

From the reconstructed data, a skymap – a histogram of the sky containing the number of events originating from each location and associated errors – is formed. These skymaps are binned in units of 0.1 deg and cover the viewable sky. All events are recorded in the J2000 epoch. Each recorded skymap contains a signal map and a background map which contain the measured counts on the sky and the background expectation respectively. The skymaps are constructed in independent bins of energy parameter $\mathcal{F}$ which is defined below in Equation 3.

The hadronic background flux is stable in time at TeV energies because TeV cosmic-rays originate from distant sources and propagate diffusively in Galactic magnetic fields. Therefore, the TeV hadronic background is not strongly affected by local variations such as solar activity. Instead, the rate and angular distribution of events is dominated by variations in the atmosphere and the detector. The background computation technique described below is intended to measure and correct for these changes.

The panels of Figure 1 demonstrate an example of the background computation in a single declination band. We represent the background rate $F(\tau, h, \delta)$ as a function of sidereal time τ and declination δ and local hour angle h. To great precision, $F(\tau, h, \delta)$ can be separated into two independent terms, $R(\tau) \cdot \varepsilon(h, \delta)$, where $R(\tau)$ is the all-sky event rate and $\varepsilon(h, \delta)$ is the local angular distribution of events.

Even large changes in $R(\tau)$, due to trigger threshold changes for example, lead to only small changes in the angular distribution of events on the sky, $\varepsilon(h, \delta)$. We exploit this feature of atmospheric showers to compute the background $B(\alpha, \delta)$ in celestial coordinates right-ascension, α, and declination, δ. The technique begins with the definition of an integration duration. For most data, the integration duration is two hours but when looking at rare events (very hard cuts) the integration duration is 24 hours. We acquire data for the integration duration and form the efficiency map $\varepsilon(h, \delta)$. This efficiency map is a normalized probability density function which indicates

from where, in local detector coordinates, events arrive. The final background estimate for this integration period is the direct convolution of the efficiency map with the rate.

$$B(\alpha,\delta) = \int \varepsilon(h,\delta) \cdot R(\alpha - h)dh \tag{1}$$

We refer to this method as "Direct Integration" since the local event distribution is measured and convolved with the detector's all-sky event rate. The time-independence of $\varepsilon(h,\delta)$ and the spatial-independence of $R(\tau)$ is key because we can use data from the entire integration duration in the computation of ε and data from the whole sky in the calculation of R. This method has been reliably demonstrated to estimate backgrounds with systematic errors of a few parts in 10^{-4}. The limiting systematic error is due to real non-uniformities in the cosmic-ray background.

After computing the background estimate $B(\alpha,\delta)$, we can take the signal map $S(\alpha,\delta)$, which is just a histogram of arrival directions and compute the excesses by computing $S(\alpha,\delta) - B(\alpha,\delta)$ in bins of α and δ.

2.1. A5: Gamma/Hadron Separation Parameter

We use an event parameter $A5$ to statistically discriminate air showers induced by gamma rays from those induced by hadrons. $A5$ is defined as

$$A5 = 400 \cdot \frac{\mathcal{F} \cdot \zeta(\mathrm{t}) \cdot \mathrm{F_{fit}}}{\mathrm{MaxPE_{MU}}}, \tag{2}$$

The parameter $\mathcal{F}$ measures the size of an event and is defined as

$$\mathcal{F} = \frac{N_{AS}}{N_{AS}^{live}} + \frac{N_{OR}}{N_{OR}^{live}}, \tag{3}$$

where N_{AS}/N_{AS}^{live} is the fraction of live PMTs in the top layer (or air-shower layer) which participated in the event and N_{OR}/N_{OR}^{live} is the fraction of live outriggers to participate in the event. The $\mathcal{F}$ parameter functions is an estimate of the event's energy and is described more in Section 3. The parameter $\mathrm{F_{fit}}$ is a parameter of the shower-fitting algorithm indicating what fraction of the PMTs registered times close to the fitted shower plane. $\mathrm{MaxPE_{MU}}$ is the number of photo-electrons recorded in the hardest-hit channel from the bottom layer of the experiment. The parameter $\zeta(\mathrm{t})$ is a few percent run-dependent correction to $\mathrm{F_{fit}}$. The distribution is seen to vary systematically in the data depending on unmodeled factors like changes in the calibration. The $\zeta(\mathrm{t})$ is a correction to take out this variation in F_{fit}. The $\mathrm{MaxPE_{MU}}$ in the denominator of $A5$ is expected to be typically larger for hadron-induced air showers because the penetrating particles

illuminate the bottom layer of the experiment. This means that $A5$ is typically larger for gamma-ray induced showers with the same number of particles reaching the ground. The numerator of A5 increases with the size of the event to account for the fact that we expect more light in the bottom layer when the event is larger and have to take out the dependence on the overall size of the event. The overall scaling factor of 400 gives A5 typical values between 1 and 10. Figure 2 shows the distribution of A5 for events in a small circle around the Crab and the separation that A5 provides.

2.2. Event Weighting

The $A5$ parameter provides separation between gamma rays and hadrons primarily because of the higher characteristic value for gamma-ray sources. To maximize the statistical significance when searching for sources, we assign each event a weight based on its $A5$ value and the signal-to-background expectation for a Crab-like source for events with that $A5$. A different set of weights is used for each $\mathcal{F}$ bin. In this approach, more-gamma-like events are counted with a higher weight than less-gamma-like events. A hard cut on the gamma/hadron parameter, which is used for the 3 highest $\mathcal{F}$ bins, is simply a step function weight. Weighted skymaps are constructed from data in 9 $\mathcal{F}$ bins between $\mathcal{F}$ of 0.2 and 2.0 in steps of 0.2.

In addition to the $A5$ weighting for gamma/hadron separation, events are given a weight to account for the angular resolution of the instrument. For a given source position hypothesis, an additional weight is applied to each event which is a function of the angular distance from the source position to the reconstructed event position. We assume a 2-dimensional Gaussian as the form of the angular resolution function, where the resolution depends on the event energy parameter, $\mathcal{F}$, and ranges from 1.2° for small $\mathcal{F}$ events to 0.35° for large $\mathcal{F}$ events.

2.3. Probability Estimation

In the absence of weighting, events from signal and background samples are compared and a probability for the observed data under the null hypothesis can be reliably computed using Equation 17 of Li & Ma (1983). When weighting events rather than simply counting them, we complicate the calculation of the expected fluctutions. In the large N limit, this problem has been solved. If one records not just the sum of the weights, $N = \sum_i w_i$, but also the sum of the squares of the weights, $N_2 = \sum_i w_i^2$, the error in N is computed as $\delta N = \sqrt{(N_2)}$.

In the small N limit however, the $\delta N = \sqrt{(N_2)}$ approximation breaks down, hence the advantage of the approach of Li and Ma who derived their probability equation assuming Poisson fluctuations. Poisson distributions take discrete values (integers), unlike continuous Gaussian distributions. Fay & Feuer (1997) point out that the Poisson distributions can be reliably approximated as a continuous envelope function described by a single parameter, which for a sum of weights is $N^{eff} = \frac{N}{\sqrt{N_2}}$. Since fluctuations are well approximated as Poisson in N^{eff}, we can rewrite the Li

and Ma expression for significance of an observed result as

$$S = \sqrt{2}\{N_{on}^{eff} ln[\frac{1+\alpha}{\alpha}(\frac{N_{on}^{eff}}{N_{on}^{eff}+N_{off}^{eff}})] + N_{off}^{eff} ln[(1+\alpha)(\frac{N_{off}^{eff}}{N_{on}^{eff}+N_{off}^{eff}})]\}^{1/2}, \quad (4)$$

where

$$N_{on}^{eff} = \frac{\sum_i w_{on,i}}{\sqrt{\sum_i w_{on,i}^2}} \quad (5)$$

and

$$N_{off}^{eff} = \frac{\sum_j w_{off,j}}{\sqrt{\sum_j w_{off,j}^2}}, \quad (6)$$

and α is the usual ratio of the signal and background exposure. We have studied this approach both through examination of data and with Monte Carlo simulations and found it to be reliable even in the regime of small statistics, $N^{eff} \sim 1$. Figure 3 shows the significance distribution for the Milagro sky. Since most of the sky has no gamma ray sources, significances are distributed normally. The fitted mean between $\pm 2\sigma$ is -0.013σ and the width is 0.996σ. This is high-level confirmation that the significance calculation is correct. The high-significance tail to this distribution is due to the presence of real sources in the sky. Figure 4 shows the final significance map in the region of the Crab. The significance at the Crab location is 17.2 standard deviations (σ). This figure includes all data over the 8-year operation of Milagro. Only data taken after the outriggers were added are used to measure the energy spectrum in this paper.

3. Energy Estimation

When a cosmic ray or gamma ray interacts in the atmosphere the amount of energy detected at the ground depends on the energy of the primary particle and the depth of the initial interaction. Since the Milagro detector is a large-area calorimeter, it is possible to measure the energy reaching the ground level with a relatively small error (~20%). However, fluctuations in the longitudinal development of air showers - due primarily to fluctuations in the depth of the initial interaction - limit the resolution of EAS arrays. Gamma rays of a given energy that penetrate deeply (a few radiation lengths) into the atmosphere deliver substantially more energy at the ground level than showers of the same energy that that interact at the top of the atmosphere. These fluctuations are log-normal (Smith 2008) and dominate the energy resolution for EAS arrays such as Milagro. Data from September 2005 to March 2008 have been used in determining the energy spectrum because the outriggers are needed to provide a dynamic range spanning 1 to 100 TeV. In this dataset, the statistical significance of the Crab is 13.5 standard deviations.

3.1. The $\mathcal{F}$ Parameter

Figure 5 shows the typical dependence of $\mathcal{F}$, defined in Equation 3, on the primary particle energy. We note that a single $\mathcal{F}$ bin covers a wide range of energies and that these energies overlap significantly. Consequently there is no advantage to a finer segmentation than the 9 bins chosen.

$\mathcal{F}$ is well-modeled by the simulation as seen in Figure 6. Shown is the experimentally-measured $\mathcal{F}$ distribution for background cosmic-rays with the simulation expectation overlaid. The gamma-ray enhancing event weights from Section 2.2 have been used as a way to probe the data and simulation agreement under the same conditions as eventual gamma-ray spectral measurements. Note that the inclusion of the gamma-ray weights significantly restricts the number of simulation events surviving to the highest $\mathcal{F}$ bins, where the gamma/hadron separation performs the best. The weights are, after all, designed to de-emphasize hadronic events. The expected background passing rate above $\mathcal{F}$ of 1.6 cannot be reliably estimated since no simulated background events survive the weighting.

3.2. Spectral Fitting

Since the energy resolution of Milagro is broad, typically 50%-100%, the energy distribuion expected in a $\mathcal{F}$ bin is dependent on the spectral assumptions. For this reason, we perform all of the spectral fits in the $\mathcal{F}$ space: For each spectral hypothesis, we simulate the expected $\mathcal{F}$ distribution and evaluate the goodness of fit based on the χ^2 statistic.

We perform spectral fits to a generalized assumption for spectral shape described by a power law with an exponential cutoff.

$$\frac{dN}{dE}(I_0, \alpha, E_{\rm cut}) = I_0(\frac{E}{E_0})^{-\alpha} \exp(\frac{-E}{E_{\rm cut}}) \tag{7}$$

In this equation, I_0, α and E_{cut} are fit parameters for the flux, spectral index and cutoff energy respectively. The E_0 parameter is not fit but rather is chosen so that the χ^2 contours of the fit variables are de-correlated. This functional form has the benefit that it intrinsically models a pure power law hypothesis when E_{cut} is above a few hundred TeV and we can test a pure power law hypothesis and a power law with an exponential cutoff hypothesis with one χ^2 computation.

The fit is performed by computing χ^2 for a given $\mathcal{F}$ distribution defined as

$$\chi^2(I_0, \alpha, E_{\rm cut}) = \sum_{i=\mathcal{F}\ bins} \frac{(P_i(I_0, \alpha, E_{\rm cut}, \text{Declination}) - M_i)^2}{\delta P_i^2 + \delta M_i^2}. \tag{8}$$

Here P and M are the sum of the predicted and measured sum of weighted events per day from the Crab and δP and δM are the error in P and M respectively. We have only considered statistical errors in the estimation of χ^2. Notice that since the value of P depends on the zenith

angle of the source as it transits and the distribution of zenith angles averaged over a transit is the same for all sources with the same declination, the predicted daily weight sum depends on the declination of the source in addition to the hypothesized spectral parameters.

The expected weighted excess is computed for discrete values of α between 1.5 and 3.5 in steps of 0.025, $log_{10}(E_{cut})$ between 0 and 3 in steps of 0.05. I_0 was scanned over a range between 0.1 and 4.5 times the nominal pure power law Crab flux measured by HESS (Aharonian et al. 2006) in steps of 0.05. The values are tabulated and the best fit spectrum is computed by minimizing χ^2.

Section 4 summarizes the results of this technique applied to the excess from the Crab Nebula and to the background cosmic-ray population as a cross-check.

4. Results

The success of our technique depends on the simulation to reliably describe the response of the instrument. Below 20 TeV, the energy spectrum of the Crab has been well measured by IACTs. In the range from 20 TeV to 100 TeV the data are limited and somewhat contradictory. We can however test the energy estimation by fitting the spectrum of the hadronic background as a cross-check of the method.

4.1. Systematic Effects

The spectrum of the hadronic background has been well measured by a series of balloon-based spectrometers as well as ground-based air shower detectors. See Particle Data Group et al. (2008) for a comprehensive review. While the simulation of hadronic interactions introduces a systematic error that is not present in simulated gamma-ray cascades, comparisons with hadronic data are nevertheless a useful verification of the simulation. A single day of data is sufficient to fit the cosmic-ray background spectrum, so reliable and accurate daily fits to the cosmic-ray spectrum serve as a measure of the stability of the energy response of the instrument.

The hadronic background is composed of numerous species. Protons dominate the flux, accounting for about 60% of the triggers in Milagro, but helium ions at about 30% and heavier element at about 10% also make important contributions. We have simulated the 8 hadronic species with the largest contribution: H, He, C, O, Ne, Mg, Si and Fe. The ATIC spectrometer has measured both the spectrum and the composition of multi-TeV cosmic rays and found different spectra for the different species. We simulate the 8 species listed with their spectra measured by ATIC (Panov et al. 2006; Ahn et al. 2006) and fit to an overall offset in the spectral index ($\Delta\alpha$) and a flux scale factor (S) where $\Delta\alpha$=0 indicates that the spectrum was measured to be exactly equal to the ATIC spectrum, $\Delta\alpha > 0$ indicates a steeper spectrum and $\Delta\alpha < 0$ indicates a flatter spectrum. Similarly, S=1 indicates an agreement with the predicted flux, $S < 1$ indicates that

Milagro measures a flux that is less than the the predicted flux and $S > 1$ indicates a greater flux than predicted.

Recall that the eventual gamma-ray fits are performed using events weighted by the gamma-ray selection weights from Section 2.2. In order that the study of cosmic-ray fits are subjected to the same systematic effects that may be present in the gamma-ray analysis, we use the same event weighting for the cosmic-ray fits, with the consequence that the majority of the cosmic-ray events are given small weight and cosmic-ray showers which appear similar to the gamma rays receive the most weight.

Figure 7 shows the fit cosmic ray flux scaling and spectral index as a function of time. E_0 was chosen to be 10 TeV for these fits. The cosmic ray index varies by less than ± 0.1 over the time shown. The overall flux scaling changes as the operational conditions of the experiment change. Many of these changes are not included in the simulation. Departures from the average are rare and suggest a systematic uncertainty in the total flux of sources close to the (Abdo et al. 2007) of 30% that has been estimated before.

The instability of the cosmic-ray fit over time is due to real $\sim 10\%$ changes in the $\mathcal{F}$ distribution of the data over time. These changes can be seen easily using the background cosmic-ray data which have small statistical errors. Figure 8 summarizes our uncertainty in the $\mathcal{F}$ distribution based on variations observed in the experimental data. For each of a set of data runs covering the observation period, we compute the $\mathcal{F}$ distribution of the background data. For each bin of $\mathcal{F}$ we quantify the width of the distribution of weighted event rates in that bin across the different runs as the 68% spread around the median. The fractional width of these distributions for each $\mathcal{F}$ are shown as the darkest band in Figure 8. Some of the run to run variation is due to an overall scaling difference between the runs. If we normalize the $\mathcal{F}$ of each run to unit area and re-do the calculation of the spread across the runs, we get the darker gray band in Figure 8. It is naturally somewhat smaller than the darkest band because variation that can be attributed to overall scaling has been taken out. Finally the lightest gray band shows the fluctuations expected due to purely statistical effects and we can see that there is a fundamental uncertainty due in the $\mathcal{F}$ distribution due simply to statistically significant differences in different days of data at the level of about 10%. This variation is due to real and unmodeled changes in the detector calibration, configuration and operating conditions.

4.2. Spectrum of the Crab

Applying the method of Section 3 to the statistical excess from the Crab Nebula, we can determine the spectrum of the Crab Nebula. The χ^2 space that is spanned by the three fitting parameters from Equation 7 is scanned to find the global minimum. To fit a simple power law or to test a number of specific hypotheses motivated by measurements from other experiments, one of the parameters can be fixed to the assumed value and the minimum χ^2 is then found over the

corresponding subset of the fit space.

To begin with, we fit the Crab spectrum under the hypothesis that the spectrum is a pure power law. That is to say that the $E_{\rm cut}$ of Equation 7 is much higher than the Milagro sensitivity. The best fit occurs at $I_o = (6.5 \pm 0.4_{\rm (stat)}) {\rm x} 10^{-14} ({\rm cm}^2 \cdot {\rm s} \cdot {\rm TeV})^{-1}$ and $\alpha = 3.1 \pm 0.1_{\rm (stat)}$ with E_0 of 10 TeV. For this hypothesis, we obtain a χ^2 of 24.1 with 7 degrees of freedom. The contours of the χ^2 function are ellipsoidal in the space of the fit parameters indicating very little correlation in the fit parameters. Assuming this hypothesis is right, we expect to have only a 0.1% probability to observe a χ^2 by chance. The moderate failure of the two-parameter model to fit the observed data is robust even if we artificially inflate the error bars in the data by 10% (added in quadrature) to allow for our systematic uncertainty in the rate of events in a given $\mathcal{F}$ bin. With the artificially inflated error bars, the χ^2 improves to 21.7 which corresponds to a chance probability of 0.3%. Figure 9 shows the $\mathcal{F}$ distribution for the Crab with our best-fit pure power law hypothesis overlaid.

An independent analysis of the Milagro data was done (Allen 2007) utilizing a different algorithm to estimate the gamma ray energy of each event which depended on: the core distance of the air shower from the center of the Milagro pond, the reconstructed zenith angle of the air shower primary, and the measured number of PMTs in the top layer and outrigger array. Gamma rays were distinguished from cosmic rays using the compactness parameter (Atkins et al. 2003) rather than $A5$. The fitted values are consistent with the fits obtained with $\mathcal{F}$ and A5 with somewhat larger error bars. The agreement indicates that our reported fit is robust with respect to energy algorithm and hadron rejection parameter.

We next consider a hypothesis of a power law, with an exponential cutoff. This is Equation 7 where $E_{\rm cut}$ is allowed to vary. With this additional free parameter, the χ^2 improves to 12.1 with 6 degrees of freedom. This corresponds to a chance probability of 6%. At the location of the best fit, $I_o = (2.5^{+0.7}_{-0.4({\rm stat})})$ x $10^{-12} ({\rm cm}^2 \cdot {\rm s} \cdot {\rm TeV})^{-1}$ with $\alpha = 2.5 \pm 0.4_{\rm (stat)}$ and $E_{\rm cut} = 32^{+39}_{-18({\rm stat})}$ TeV. For this fit E_0 was set to 3 TeV. Figure 11 shows projections of the 1 and 2σ allowed regions in the plane of our three fit variables. The somewhat broad allowed range of spectral indices and cutoff energies is due to a fundamental ambiguity in the Milagro data that a soft spectrum is hard to distinguish from a harder spectrum with an exponential cutoff. Fixing the low-energy spectral index to the values between 2.4 to 2.6, as measured by other experiments, gives a 1σ allowed range for the cutoff energy of between 20 and 40 TeV.

Neither of the two spectral assumptions is preferred strongly by fitting the Milagro data. The pure power law fit is a marginally poor fit. The addition of an exponential cutoff improves the fit. The measured fluxes are shown on Figure 10 for the two hypotheses. Regardless of which fit is chosen, the general conclusion is clear: The high-energy spectrum, above about 5 - 10 TeV, is steeper than measured by IACTs at lower energies. In the pure power-law hypothesis, this manifests itself as a measured spectrum of $\alpha = 3.1 \pm 0.1$, steeper than has been measured by, for instance, HESS of 2.4 to 2.6. The fit that allows for an exponential cutoff reproduces the low-energy spectral index measured by IACTs and this steepening at high energy is seen as an exponential cutoff at $\sim$

30 TeV.

Finally, it is interesting to note that above 30 TeV, the HESS and HEGRA data are mildly inconsistent. The HEGRA measurement continues to higher energy than the HESS data. It has been suggested (Bednarek & Idec 2011) that this discrepancy is related to the time variability observed by the Crab since HEGRA was observing earlier than HESS. The Milagro data, which represents the time-average over 3 years of data, indicates a spectrum between the data of HESS and HEGRA.

5. Conclusions

The Crab Nebula is the brightest northern hemisphere TeV source and has been extensively measured by IACTs above 1 TeV. The Milagro measurement of the energy spectrum of the Crab has been presented. A background rejection parameter ($A5$) has been described and shown to distinguish between gamma ray and hadronic primaries in the detector. We have presented the weighting and background estimation and background subtraction techniques used to extract the Crab signal, giving a 17σ over the lifetime of the experiment.

The size of an air shower at ground represented by the fraction of PMTs in the Milagro experiment that detect a signal (the $\mathcal{F}$ parameter), is a suitable variable for measuring the spectra of primary TeV gamma and cosmic rays. The relatively simple form of $\mathcal{F}$ is justified because the dominant effect contributing to the energy resolution of Milagro is fluctuations in the depth of first interaction of the primary particles and not in the measurement of the energy reaching the ground. The parameter is well modeled in the simulation as observed by studying the cosmic ray background.

The energy spectrum of gamma rays from the Crab between 1 and 100 TeV has been measured by fitting the observed $\mathcal{F}$ distribution of the Crab with expectations from simulation. A steepening of the spectrum above about 5-10 TeV with respect to measurements by IACTs at lower energies has been measured.

The experiment observes the entire overhead sky, the data and analysis technique presented here for the Crab observations can be used to measure the flux and spectral properties of the other sources in the Milagro catalog. The agreement seen on the Crab as a calibration source justifies confidence in measurements of other sources.

We gratefully acknowledge Scott Delay and Michael Schneider for their dedicated efforts in the construction and maintenance of the Milagro experiment. This work has been supported by the National Science Foundation (under grants PHY-0245234, -0302000, -0400424, -0504201, -0601080, and ATM-0002744), the US Department of Energy (Office of High-Energy Physics and Office of Nuclear Physics), Los Alamos National Laboratory, the University of California, and the Institute

of Geophysics and Planetary Physics.

REFERENCES

Abdo, A. A., et al. 2011, Science, 331, 739

—. 2007, ApJL, 658, L33

—. 2009, ApJS, submitted (arXiv:0902.1340)

Aharonian, F., et al. 2004, ApJ, 614, 897

—. 2006, A&A, 457, 899

Ahn, H. S., et al. 2006, Advances in Space Research, 37, 1950

Aielli, G., et al. 2010, ATel, 2921

Aliu, E., et al. 2008, Science, 322, 1221

Allen, B. 2007, PhD thesis, University of California, Irvine

Amenomori, M., et al. 2009, ApJ, 692, 61

Atkins, R., et al. 2003, ApJ, 595, 803

—. 2000, Nuclear Instruments and Methods in Physics Research A, 449, 478

Bartoli, B., et al. 2011, ApJ, 734, 110

Bednarek, W., & Idec, W. 2011, MNRAS, 414, 2229

Celik, O. 2008, in International Cosmic Ray Conference, Vol. 2, International Cosmic Ray Conference, 847–850

Fay, M. P., & Feuer, E. J. 1997, Statistics in Medicine, 16, 791

Gaensler, B. M., & Slane, P. O. 2006, ARA&A, 44, 17

Li, T.-P., & Ma, Y.-Q. 1983, ApJ, 272, 317

Panov, A. D., et al. 2006, Advances in Space Research, 37, 1944

Particle Data Group et al. 2008, Physics Letters B, 667, 1

Smith, A. J. 2008, in International Cosmic Ray Conference, Vol. 2, International Cosmic Ray Conference, 397–400

Tavani, M., et al. 2011, Science, 331, 736

Weekes, T. C., et al. 1989, ApJ, 342, 379

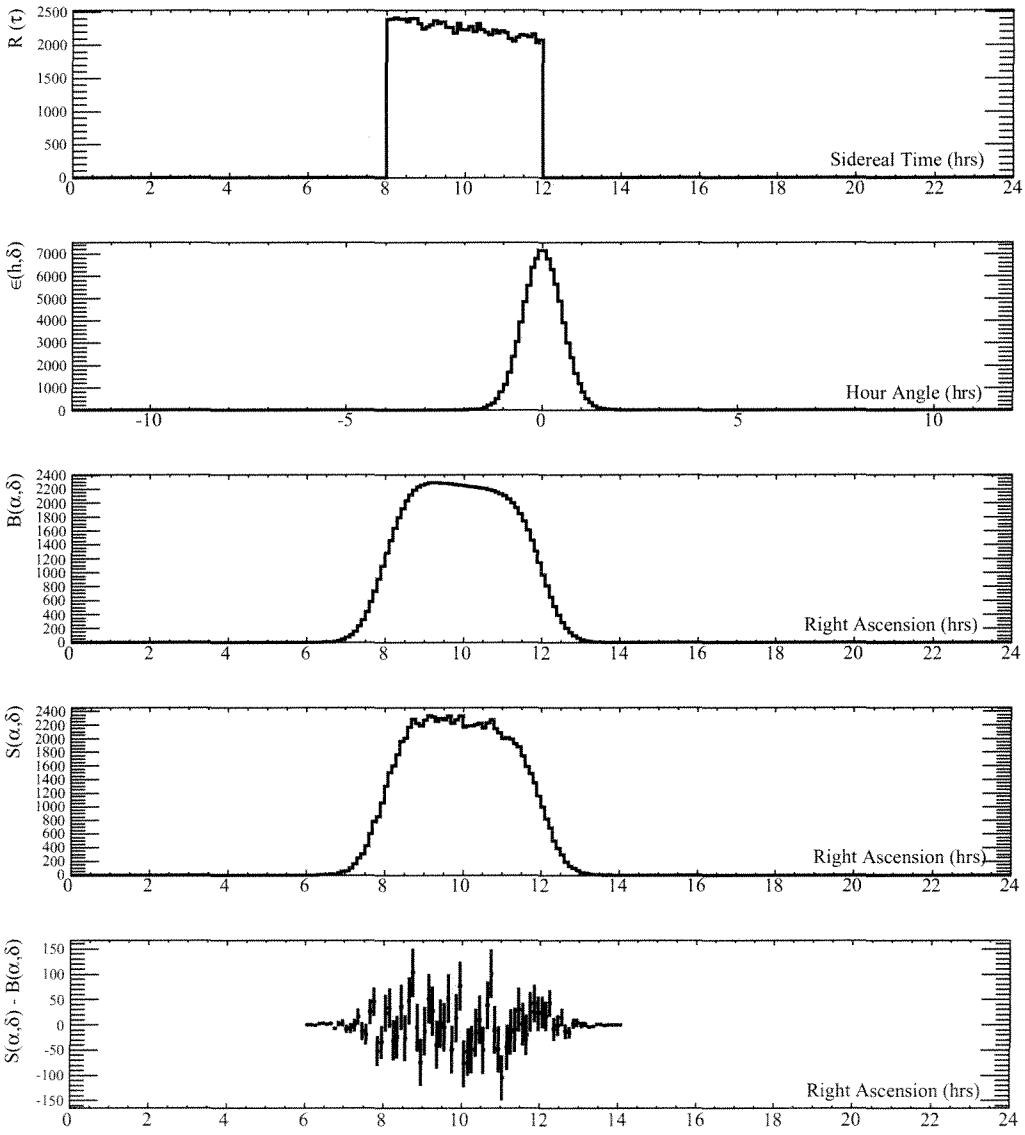

Fig. 1.— Example of the background subtraction technique in a single declination band. For display purposes, this calculation is performed with a four-hour integration instead of the standard two-hour integration. $R(\tau)$ is the all-sky event rate. $\epsilon(h, \delta)$ is the local-coordinate distribution of event arrivals and is convolved with $R(\tau)$ to arrive at $B(\alpha, \delta)$, the background estimate. $B(\alpha, \delta)$ is subtracted from the binned event arrival directions $S(\alpha, \delta)$ to arrive at the actual excess estimates.

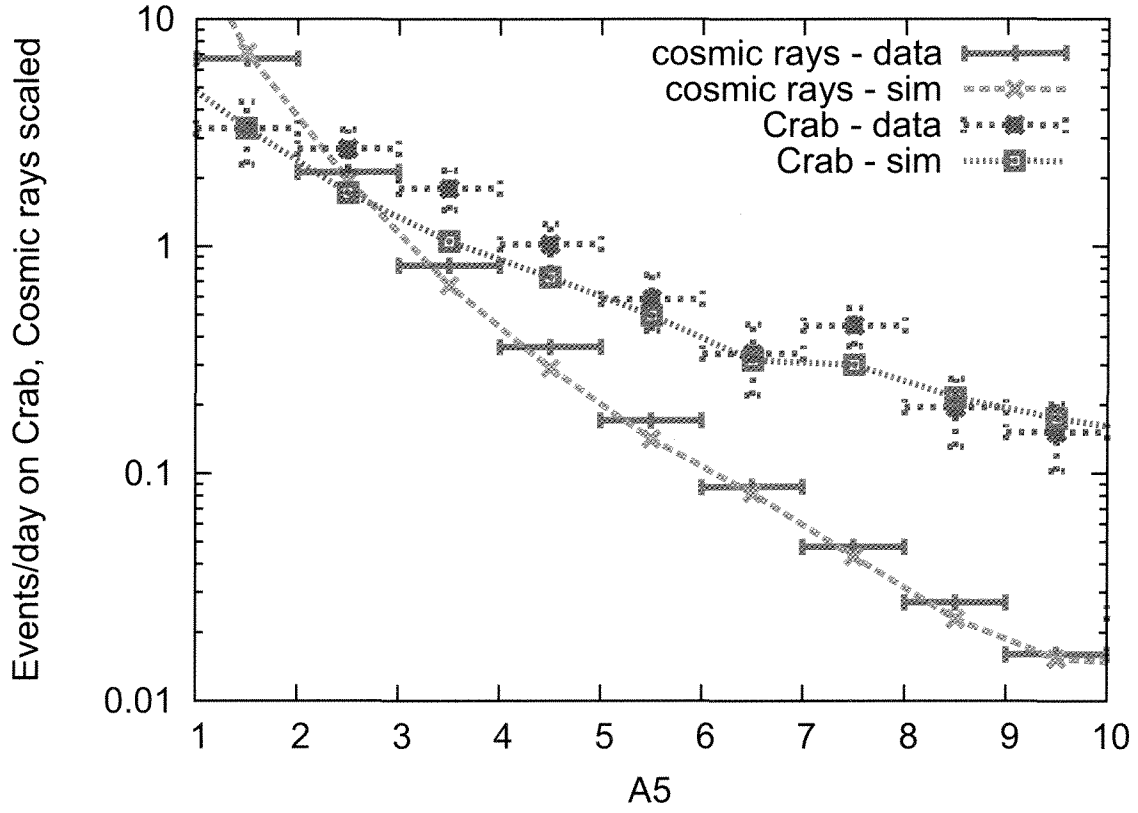

Fig. 2.— Shown is the distribution of A5 compared to simulation, both for the background cosmic rays and for the background-subtracted Crab excess. The gamma ray signal is shown in a small 0.7 degree circle around the true Crab location. The A5 parameter is used to distinguish gamma-ray events from hadronic events. A higher value of A5 indicates a higher probability than an event originated from a gamma ray.

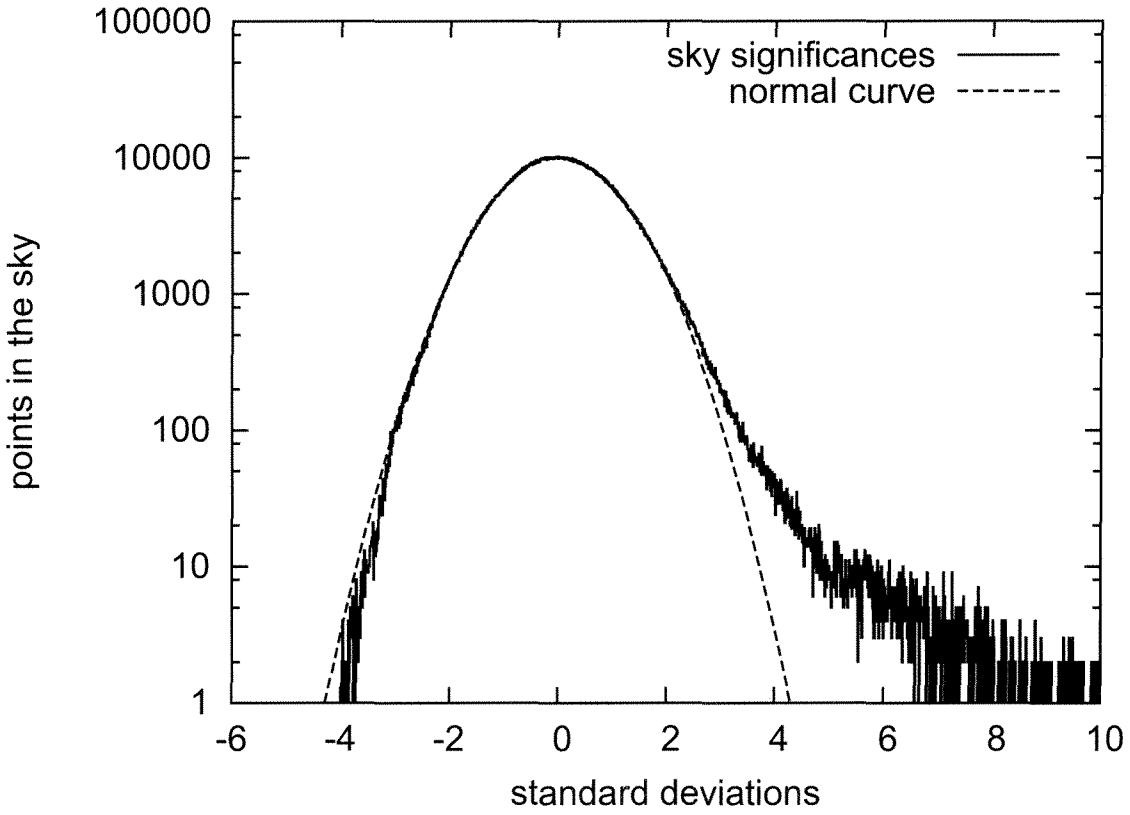

Fig. 3.— Shown is the significance distribution of independent points in the Milagro field of view. The excess of positive significance is due to the presence of sources. The central peak fits well a Gaussian of width 1 σ, indicating that the statistical significances are calculated correctly.

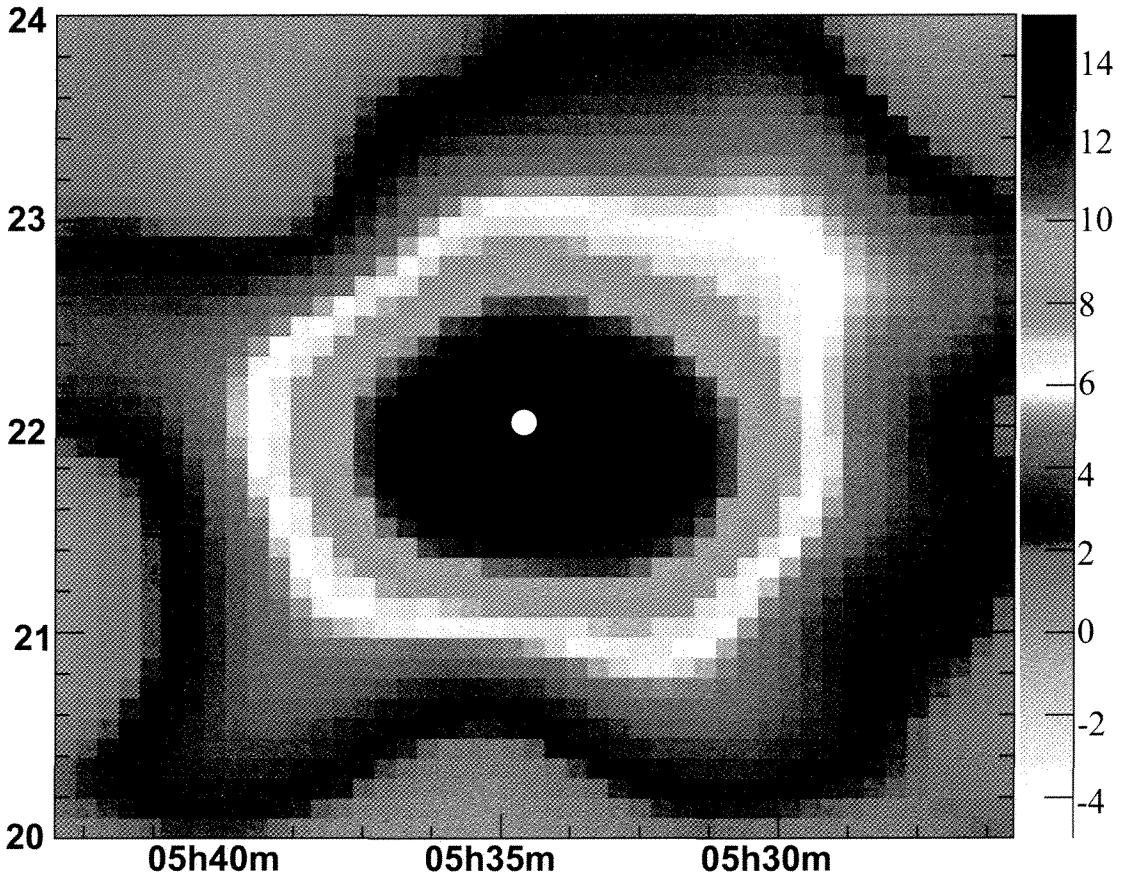

Fig. 4.— Shown is the statistical significance in the region around the Crab Nebula, indicated by the white dot. The gamma-ray-enhancing weights as well as the angular smoothing from the text have been incorporated. Data over the entire 8-year lifetime of the experiment have been used and all $\mathcal{F}$ bins have been combined. At each point in the map, the statistical significance is calculated. The smoothing causes the points to be very correlated. The significance at the location of the Crab is 17.2σ.

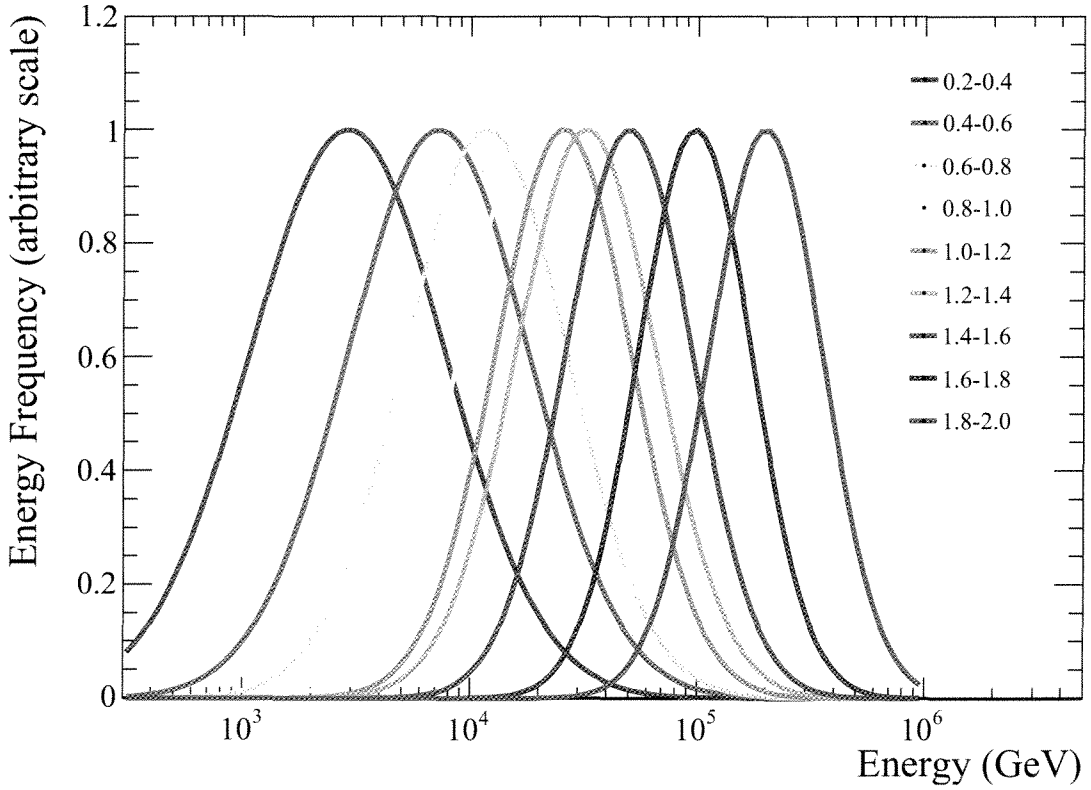

Fig. 5.— Typical dependence of $\mathcal{F}$ with energy. A source with a spectrum of 2.6 is assumed. Shown is the unit-normalized distribution of true energies for events in the indicated $\mathcal{F}$ range.

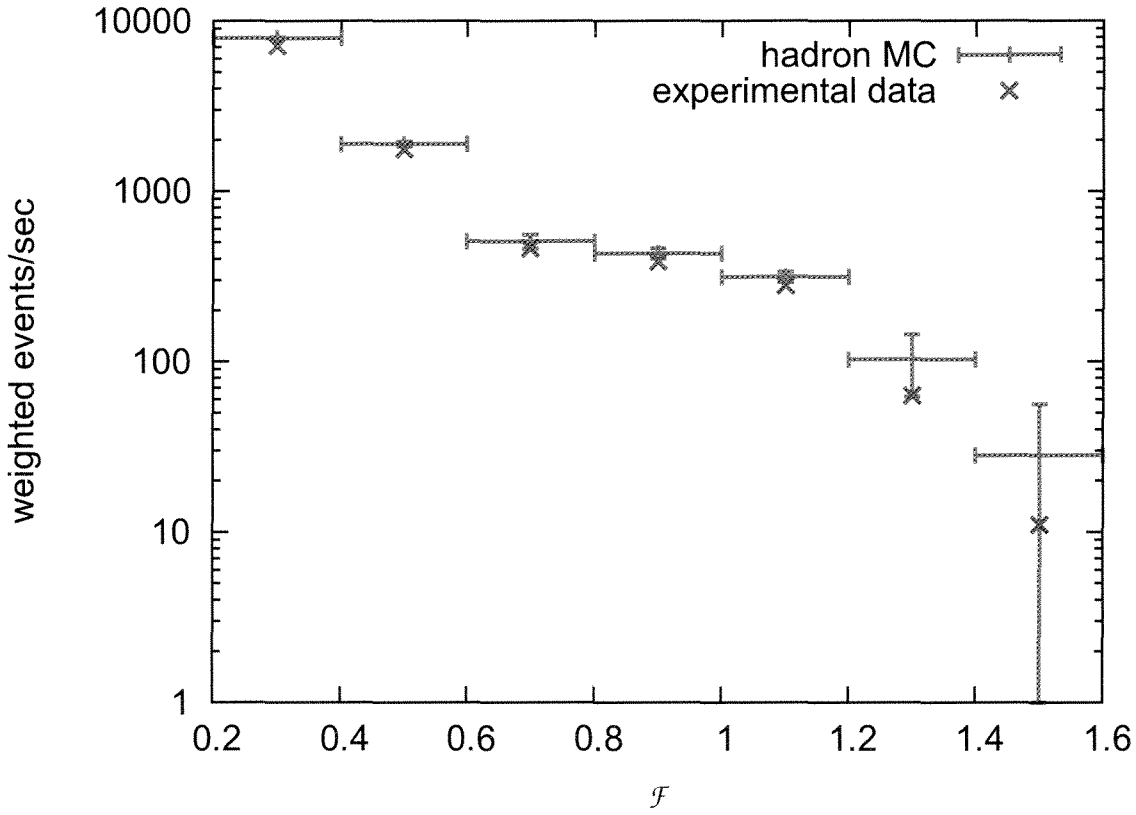

Fig. 6.— The $\mathcal{F}$ distribution of the background cosmic rays in a 2.5 degree bin at the same declination as the Crab, but offset by a few degrees in right ascension. Note that the weights from Section 2.2 have been applied in this comparison as a way to probe potential systematic biases introduced by the weighting procedure. The statistical errors in the simulation expectation for high $\mathcal{F}$ are quite large due to the weighting which leaves very few cosmic ray events with high weight in highest $\mathcal{F}$ bins.

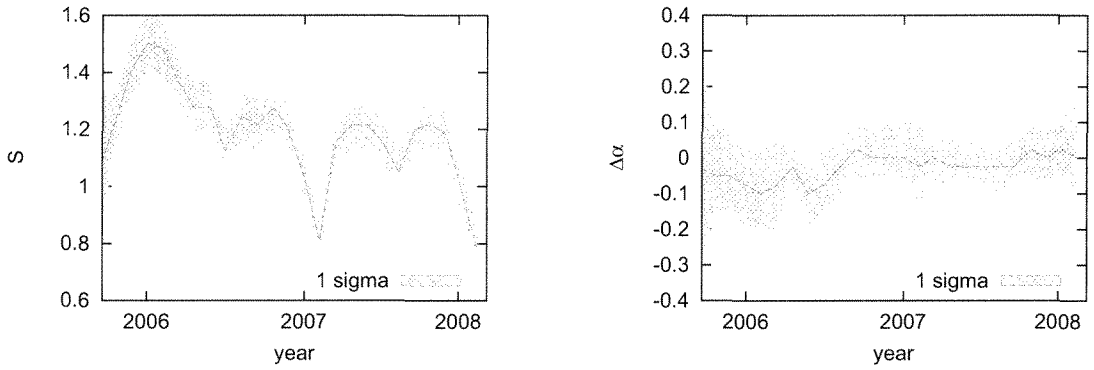

Fig. 7.— The left figure shows the fitted cosmic ray scale (relative to the simulation) as a function of time and the right figure shows the fitted cosmic ray index, as an overall steeping or flattening of the simulated spectrum. Note that $\mathcal{F}$ greater than 1.4 was not used in these fits.

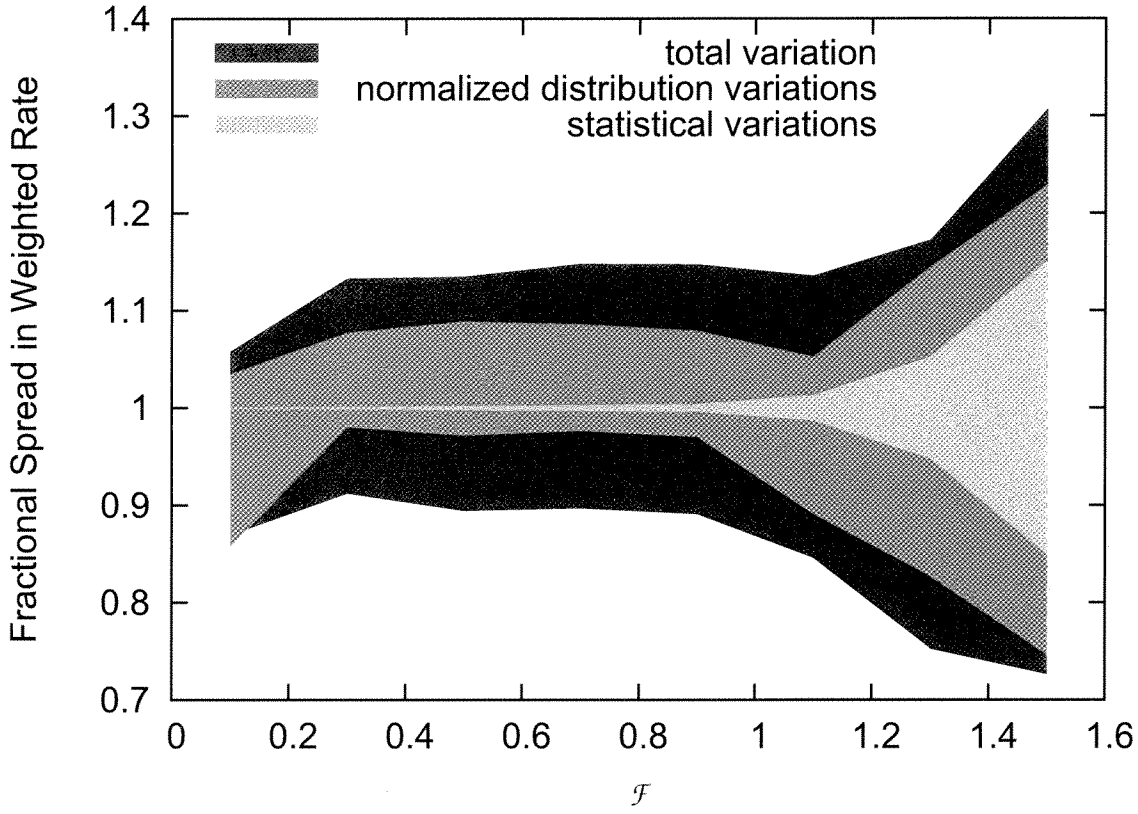

Fig. 8.— This figure quantifies uncertainty in the $\mathcal{F}$ distribution. The 68% central values for background weighted event rates going into $\mathcal{F}$ bins across different days of data acquisition are shown. Both the absolute variations are shown along with variations after normalizing the underlying $\mathcal{F}$ distributions to unit area. This indicates a fundamental $\sim 10\%$ uncertainty in the shape of the $\mathcal{F}$ distribution.

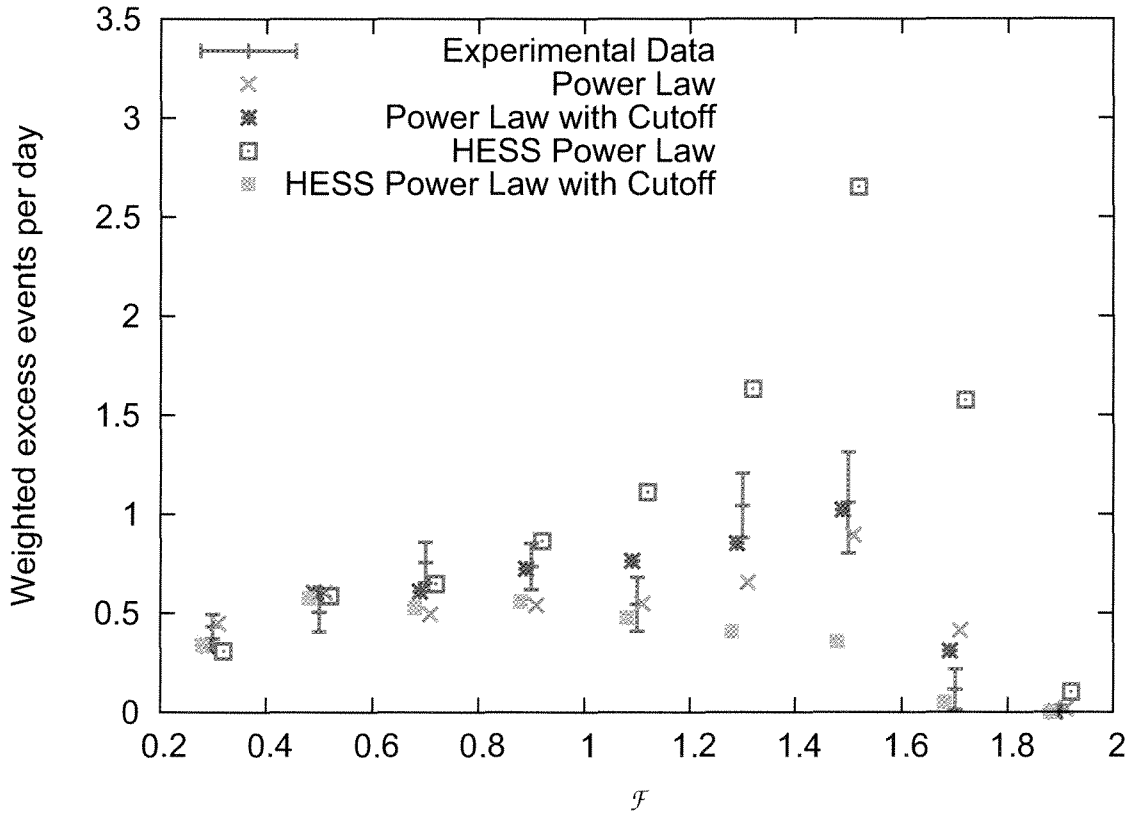

Fig. 9.— The distribution of the $\mathcal{F}$ parameter measured in data and expected from simulation for several hypotheses. The first two are the best fits to the Milagro data both with a pure power-law and power-law with an exponential cutoff. The second two show the expectations from the best HESS solutions, both for a pure power law (with a differential photon spectral index of -2.63) and including an exponential cutoff (with an index of -2.39 and a cutoff at 14.3 TeV) as reported in Aharonian et al. (2006). Note the points have been offset horizontally by a small amount for display.

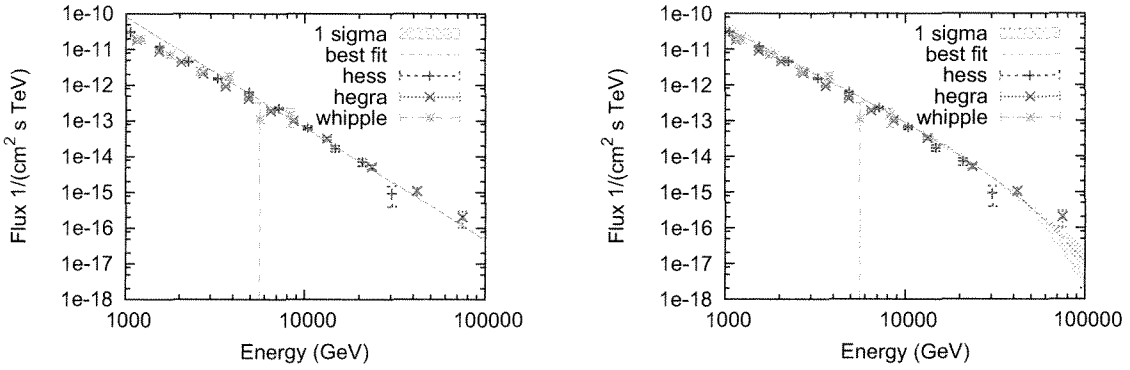

Fig. 10.— The panels display the spectrum of the Crab as measured by Milagro. The pure power law hypothesis is shown on the left and the power law with an exponential cutoff is shown on the right. The one σ regions are shown with shading and the points measured by HESS, HEGRA and Whipple are overlaid.

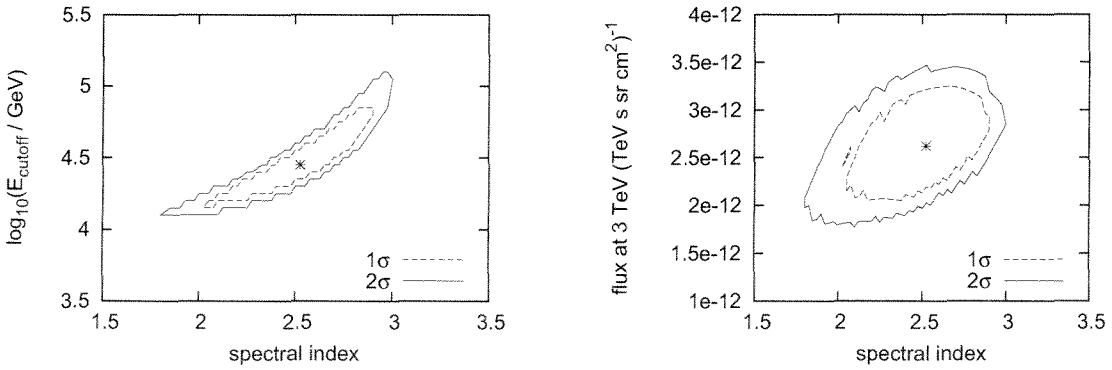

Fig. 11.— Shown are the 1 and 2σ allowed regions for the full power-law hypothesis including an exponential cutoff. The position of minimum χ^2 is indicated. The 3-d regions have been projected into planes of the three fit variables.